Modelling shear stress distribution in ice-covered streams

Check for updates

Berkay Koyuncu¹ and Trung Bao Le^{1,2}*

- ¹Environmental and Conservations Science, College of Engineering, North Dakota State University, Fargo, ND, USA
- ²Department of Civil, Construction and Environmental Engineering, North Dakota State University, Fargo, ND, USA

Abstract: Distribution of bed shear stress is the critical factor in regulating the meandering of single-thread rivers. However, the impact of ice cover on bed shear stress is largely unknown. In this study, we develop a theoretical model of cross-stream momentum balance to examine the distribution of bed shear stresses in ice-covered meandering rivers. To validate the theoretical model, field surveys were carried out in a river reach of the Red River in Fargo, North Dakota. Data monitoring was completed using an Acoustic Doppler Current Profiler to obtain time-averaged velocity profiles. Our theoretical model indicates that an ice covering develops high-shear zones near both the inner and outer banks, which might exacerbate sediment transport and enhance bank erosion. Velocity measurements confirm the results of the proposed model and demonstrate a clear impact of meandering river banks on velocity profiles and secondary flow patterns under ice cover. Based on our results, we hypothesize that ice cover increases turbulent stresses near banks, which in turn lead to the enhancement of the bed shear stress. Our work provides new insights into the impact of ice cover on bed shear stress distribution, which could play an important role in driving sediment-transport processes and the long-term morphodynamic evolution of meandering rivers seasonally covered by ice.

Most studies in river hydraulics have focused on the ice-free condition (Blanckaert and Graf 2001; Blanckaert and De Vriend 2005; van Balen et al. 2010; Constantinescu et al. 2011; Koken et al. 2013). However, the existence of ice cover during the winter season in cold regions changes flow structures (Kirillin et al. 2012; Wang et al. 2020, 2021). In comparison to the open-surface condition, ice cover increases the complexity of the threedimensional flow structures, especially the vertical velocity profiles (Teal et al. 1994; Wang et al. 2020). Hence, flow structure and dynamics in icecovered streams is still an active area of research (Demers et al. 2011). To date, the impact of ice cover on the hydrodynamic and morphological characteristics of rivers is still largely unknown (Gautier et al. 2021). Globally, the extent of river ice is tending to decrease under the impact of climate change (Yang et al. 2020). Thus, the understanding of icecovered hydrodynamics will assist in the prediction of forthcoming changes in the large-scale morphology of rivers found in cold regions (Lauzon et al. 2019).

The most common theoretical approach to address the impact of ice is the two-layer hypothesis, which assumes the independent existence of two logarithmic layers near the channel bed and the ice cover, respectively (Urroz and Ettema 1994; Wang *et al.* 2020). The presence of the logarithmic layer allows the logarithmic fitting to estimate the shear

velocity of the bed (u_b^*) (Petrie and Diplas 2016). Recently, the logarithmic fitting has been used to estimate the shear velocity of the ice layer (u_i^*) as well (Sukhodolov *et al.* 1999; Ghareh Aghaji Zare *et al.* 2016) under field conditions. However, the recent work of Guo *et al.* (2017) suggested that the two-layer hypothesis has many shortcomings, including the discontinuity of the velocity gradient. In addition, the relationship between the shear stresses on the river bed and the ice cover has not been clarified in previous studies owing to the de-coupling assumption of the two logarithmic layers.

Bed shear stress is a critical factor in regulating river morphology (Parker 1978; Nanson and Huang 2017). In classical theories of open channel flow in straight channels, the river channel is usually assumed to be infinitely wide (Devauchelle *et al.* 2022). This assumption ignores the lateral momentum transfer across a cross-section. Thus, the distribution of bed shear stress near banks due to the momentum transfer is typically not considered despite bed shear stress distribution playing a critical role in the evolution of river width (Seizilles *et al.* 2013, 2014; Métivier *et al.* 2017; Popović *et al.* 2021; Devauchelle *et al.* 2022).

The most significant location for the cross-stream momentum balance is the correspondence of river bends. Flow over a bend is characterized by an acceleration of flow velocity near the outer bank,

^{*}Correspondence: trung.le@ndsu.edu

especially at the point of the maximum channel curvature (i.e. bend apex). Under open-surface conditions, the centrifugal force gives rise to the emergence of a helical motion that directs fluid from the inner bank towards the outer bank within a cross-section (Ferreira da Silva and Ebrahimi 2017). This redistribution of momentum has been thought to be the driving force for river meandering. Under open-surface conditions, the main circulation is dominant throughout the cross-section at high flow rates (i.e. bankfull conditions) (Koyuncu and Le 2022). Under ice-covered conditions, this helical motion (secondary flow) is observed to change (Demers et al. 2011; Koyuncu and Le 2020). There is evidence suggesting that the helical cell pattern is altered as the ice cover promotes the cross-stream momentum transfer by introducing an additional helical cell near the ice layer (Demers et al. 2011). It is the formation of double-stacked secondary cells that is hypothesized to influence the secondary flow patterns under the ice cover (Urroz and Ettema 1994; Tsai and Ettema 1996; Lotsari et al. 2017). To date, it is unclear how this change affects the distribution of bed shear stress.

In this work, the impact of ice coverage on the bed shear stress distribution is investigated. First, a theoretical model is developed based on the momentum balance to identify the important parameters of the problem. We propose a relationship between the shear stresses at both the bed and ice surfaces using the cross-stream momentum balance. Second, field measurements are carried out to provide validation data for the theoretical model. The impacts of the ice cover on the vertical velocity profiles are reported. A comparison between the theoretical

model and the measured data is discussed. Finally, the applications of the proposed theoretical model for estimating bed shear stress under ice coverage are explained.

Methodology

Study area

The chosen study area is a 1.0 km-long reach of the Red River of the North (Fig. 1a), which originates in the state of North Dakota, USA. This specific location was chosen owing to the accessibility to the river surface both during open-surface and ice-covered conditions (Fig. 1b). At the end of the reach, hydrological data (i.e. water level, discharge, temperature) are collected continuously at the United States Geological Survey (USGS) Fargo station (09020104). The station is located at latitude 46° 50′ 40″ and longitude -96° 47′ 00″ (NAD27) in North Dakota, USA. The gauge is at 263 m (862.88 ft) above the datum.

The topography data for the study area were retrieved from the ND State Water Commission LiDAR data (https://lidar.dwr.nd.gov with a horizontal and vertical accuracy of 1 m and 0.2 m, respectively. The radius of curvature is 110 m and the river width is c. 38 m; accordingly, the ratio of the radius of curvature to river width is calculated as 2.9 for the bend in Figure 1a.

Field surveys

Field surveys were carried out on 2 October 2020, 10 October 2020 and 8 February 2022 in the study area



Fig. 1. (a) The Red River reach in the study area. The pedestrian bridge is located in the relatively straight portion of the reach. (b) Drone photograph of the pedestrian bridge (19 March 2022). (c) The ice holes opened along the cross-sections. Source: Satellite image: Google Earth Pro – March 2021.

Table 1. The summary of all expeditions in autumn 2020 (bridge cross-section under open surface case (OS) and bathymetry measurement) and winter 2022 (CS_1 , CS_2 , CS_3 and CS_4)

| Case | Date | Surface | $Q (\mathrm{m}^3 \mathrm{s}^{-1})$ | Elevation (m) | No. verticals | T (mins) |
|------------|------------|---------|------------------------------------|---------------|---------------|----------|
| OS | 2 Oct. 20 | Open | 23.5 | 267.22 | 13 | 10 |
| Bathymetry | 10 Oct. 20 | Open | 20.1 | 267.17 | _ | _ |
| CS_1 | 8 Feb. 22 | Ice | 11.1 | 267.05 | 6 | 4 |
| CS_2 | 8 Feb. 22 | Ice | 11.1 | 267.05 | 6 | 4 |
| CS_3^2 | 8 Feb. 22 | Ice | 11.1 | 267.05 | 5 | 4 |
| CS_4 | 8 Feb. 22 | Ice | 11.1 | 267.05 | 5 | 4 |

The hydrological data (flow discharge Q and water surface elevation) are monitored at the USGS Fargo (09020104) station. T (minutes) is the total time of measurement in each vertical/(ice hole) location.

as shown in Figure 1c. The summary of the field expeditions is shown in Table 1. A Sontek M9 Acoustic Doppler Current Profiler (ADCP) was employed for the data collection stage. The sampling frequency of the ADCP was 1 Hz with a 0.06 m vertical cell size. During all the measurements, the transducer depth was set to 0.25 m below the water surface. Depending on the case and purpose, two deployment techniques were adopted to conduct measurements: (1) moving-vessel (MV); and (2) fixed-vessel (FV) techniques. The MV deployment technique was only available for the open-surface condition while collecting the bathymetry to develop the digital terrain model (DTM). During the bathymetry collection and cross-sectional measurements, the M9 and the Hydroboard were attached to a kayak and moved on the river surface. In contrast, the FV deployment technique was used for the icecovered condition to monitor the vertical velocity profile by keeping the sensor stationary throughout the recording.

Under the open-surface condition (10 October 2020), the ADCP was towed along the entire bend to create the bathymetry (see Fig. 2a). The depth-averaged velocity was collected continuously throughout this towing process. In addition, we performed one FV measurement on 2 October 2020 on the bridge cross-section (see Fig. 2a). These datasets provide the baseline ice-free conditions.

Since the FV deployment technique (stationary technique) is the only available option for the measurements during the winter, ice holes were opened on the cross-sections (see Table 1). The most critical issue for the FV technique is that the ice thickness must be thick enough to walk on. The ice thickness was checked manually using a chisel in all cross-sections before any measurements. Measurements showed that the ice layer thickness was *c*. 0.3–0.5 m. The air temperature was at *c*. –15°C on most of our measurement days. Under this condition, the ADCP sensor is sensitive to air temperature and

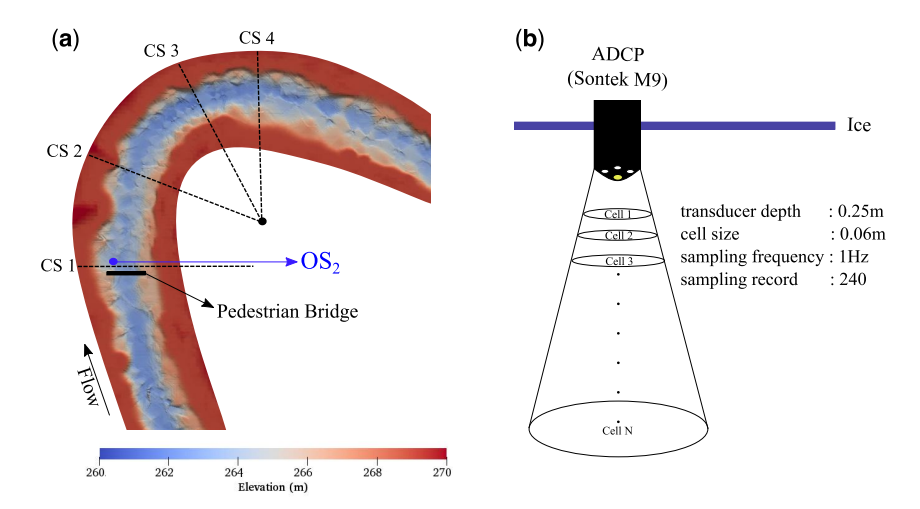


Fig. 2. (a) The locations of the cross-section CS_1 , CS_2 , CS_3 and CS_4 in February 2022. The location of CS_1 is at the bridge. The elevation of the bathymetry is shown in the UTM-14N WGS-84 coordinate system. A stationary measurement was carried out near the outer bend (OS_2) under open-surface conditions (2 October 2020) as shown in Table 1. (b) The placement of the ADCP M9 under the ice cover. Owing to the side-lobed configuration of the sensors, signal interference might occur near the river bed.

its surface can become frozen easily. The ADCP sensor also has the well-known issue of signal interference near the river bed (see Fig. 2b). Thus, it is challenging to collect data points close to the river bed and the ice cover (Demers *et al.* 2011).

The field survey in the ice-covered condition was carried out in a single day (08:00–17:00, 8 February 2022), and thus variations in the flow rate are considered negligible. Four cross-sections were selected downstream of the pedestrian bridge, CS_1 , CS_2 , CS_3 and CS_4 , as shown in Figure 2. The recording length for each ice hole is limited to T=4 minutes. We refer to a measurement at the cross-section N with a vertical line M using the notation CS_N -M.

Topography and bathymetry data processing

Since the LiDAR data do not provide the river bathymetry, it is necessary to combine the ADCP data and the LiDAR point clouds. After completing the collection of bathymetry and cross-section data, a three-dimensional model of the study area can be reconstructed. An in-house MATLAB script was written to merge the LiDAR and ADCP data using the reference water level at the USGS Fargo station. Subsequently, the final output DTM was generated, as seen in Figure 2.

Flow data processing

The raw data from the ADCP in text format were processed using our in-house MATLAB script to produce a 1 Hz time series of three velocity components $u_{\rm E}$, $u_{\rm N}$ and $u_{\rm up}$ in the east, north and vertical directions of the Universal Transverse Mercator (UTM). Therefore, the local velocity magnitude u(z, t) at a depth z and time t is computed as:

$$u(z, t) = \sqrt{u_{\rm E}(z, t)^2 + u_{\rm N}(z, t)^2 + u_{\rm up}(z, t)^2}$$
 (1)

A separate MATLAB script was used to calculate flow statistics from the time series including: (a) the depth-averaged velocity profiles; and (b) the time-averaged velocity profile for each vertical location. Following the suggestion of Petrie and Diplas (2016), the time-averaged profiles for each vertical u(z, T) and the depth-averaged value U(T) are computed as the function of averaging period T as:

$$u(z, t) = \frac{1}{T} \int_{t=0}^{t=T} u(z, t)dt$$

$$U(T) = \frac{1}{H} \int_{z=-H}^{z=0} u(z, T)dz$$
(2)

The final values of U(T) and u(z,T) correspond to the time-averaged values of the entire record. They are denoted by the depth-averaged (U_{∞}) and time-averaged $(u_{\infty}(z))$ velocities, respectively, to provide a scale to indicate the range of variability of the signals. Finally, the calculation of the shear velocities u_b^{\star} and u_i^{\star} are based on the values of $u_{\infty}(z)$ as shown in the next sections. Unless otherwise noted, the notation ∞ is dropped to simplify the discussion of the vertical velocity as u(z).

Logarithmic velocity profile

The traditional method to determine the values of u_b^* and u_b^* is to assume that there exist two logarithmic layers near the ice and the bed surfaces in the vertical velocity profile u(z) (Ghareh Aghaji Zare *et al.* 2016). The logarithmic law of a rough wall for the bed layer reads as (Shen and Lemmin 1997):

$$\frac{u(z-z_b)}{u_b^*} = \frac{1}{\kappa} \ln \frac{z-z_b}{k_s} + \beta \tag{3}$$

where $\kappa=0.39$ is the Von Karman constant, β is the additive constant ($\beta=8.5$) and $z_{\rm b}$ is the bed elevation. The parameter $k_{\rm s}$ is the roughness length. In natural rivers, this logarithmic law is typically considered valid within a distance $\delta_{\rm b}$ from the river bed. Typically, $\delta_{\rm b}$ varies from 20 to 50% of the total water depth H (Petrie *et al.* 2013; Petrie and Diplas 2016; Koyuncu and Le 2021).

The shear velocity (u_b^*) and the roughness length (k_s) are found by fitting equation (3) to the measured data $(u(z-z_b))$. A common procedure is to use the linear regression line between the measured value of $u(z-z_b)$ and $\ln(z-z_b)$ (Petrie and Diplas 2016). As the linear regression line is known, the values of u_b^* and k_s are computed as:

$$u_{\rm h}^{\star} = \kappa m \tag{4}$$

$$k_{\rm s} = \exp\left[8.5\kappa - \frac{\gamma}{m}\right] \tag{5}$$

Here, γ and m are the intercept point and the slope of the best-fit regression line, respectively.

It is common to use wall units to describe the fitting process using u_b^* and v to form the velocity and viscous length scales. The vertical distance from the river bed $z - z_b$ and the dimensionless velocity profile $u^+((z - z_b)^+)$ are expressed in terms of wall units as:

$$(H - |z|)^{+} = \frac{(H - |z|)u_{b}^{*}}{v}$$
 (6)

$$u^{+}((H-|z|)^{+}) = \frac{u(H-|z|)}{u_{b}^{*}}$$
 (7)

A similar fitting procedure can be carried out to define the shear velocity for the ice layer using the value of |z|:

$$|z|^+ = \frac{|z|u_i^*}{v} \tag{8}$$

$$u^{+}(|z|^{+}) = \frac{u(|z|)}{u_{i}^{*}} \tag{9}$$

To perform the fitting process, data points must be available in the logarithmic layer. The minimum number of available points is selected as five in the current study. The agreement between the linear regression line and the measured data must also satisfy the following criteria: (1) a correlation coefficient $R^2 > 0.70$; (2) a positive shear velocity u_b^{\star} , $u_i^{\star} > 0$; and (3) a realistic value of k_s (0.001 m < k_s < 10 m). The fitting process is rejected if one of these conditions is not met. The details of the fitting procedure can be found in Koyuncu and Le (2022).

Quartic profile for asymmetrical flows

The quartic profile of Guo *et al.* (2017) is formulated using the relative distance η , which is defined as $\eta = (2(H - |z|)/H)$. The maximum velocity location in each vertical (z_{max}) is defined in terms of its relative distance as $\eta_{\text{max}} = (2(H - |z_{\text{max}}|)/H)$.

The dimensionless parameter λ is used to represent the asymmetry of the flow profile. It is assigned by the fitting as:

$$\lambda = \sqrt{\frac{2}{\eta_{\text{max}}} - 1} \tag{10}$$

Here $\lambda = (u_{\rm i}^{\star}/u_{\rm b}^{\star})$ quantifies the asymmetry of shear stress on the top $(u_{\rm i}^{\star})$ and bottom $(u_{\rm b}^{\star})$ surfaces. Therefore, the value of λ is important in determining the shape of the velocity profile.

The location of the zero shear stress plane (η_c) typically does not coincide with the maximum velocity location (Hanjalić and Launder 1972). In practice, they are relatively close (Guo 2017). To simplify the fitting procedure, we assume that $\eta_c \approx \eta_{\text{max}}$. Thus, this location can relate to λ as $\eta_c \approx \eta_{\text{max}} \approx (2/(1 + \lambda^n))$ with $u_c \approx u_{\text{max}}$.

The quartic solution finds the best-fit velocity profile (u_f) to the measured data. u_f can be written in terms of its dimensionless form u^+ with the help

of the bed shear velocity u_b^* as:

$$\frac{u_{\rm f}(\eta)}{u_{\rm h}^{\star}} = u^{+}(\eta) \tag{11}$$

Therefore, the bed shear velocity is used to provide a dimensionless profile $u^+ = u/u_b^*$. For example, the critical velocity at the critical depth η_c is non-dimensionalized as $u_c^+ = u_c/u_b^*$.

It is suggested that the dimensionless velocity profile (u^+) follows the analytical solution (Guo *et al.* 2017):

$$u^{+}(\eta) = u_{c}^{+} + \phi(\eta)$$
 (12)

Here the velocity profile function $(\phi(\eta))$ is derived for an infinitely long and straight channel as:

$$\phi(\eta, \lambda) = \frac{1}{\kappa} \left[\ln\left(\frac{\eta}{\eta_{c}}\right) + \lambda \ln\frac{2 - \eta}{2 - \eta_{c}} - \frac{1 + \lambda}{2} \right]$$

$$\ln\left[1 + \alpha \left(1 - \frac{\eta}{\eta_{c}}\right)^{2} \right] - (1 - \lambda^{n+1})\sqrt{\alpha} \left(1 - \frac{\eta}{\eta_{c}}\right)$$
(13)

where, α is an interim parameter ($\alpha = (1 - \lambda/\lambda - \lambda^{2n})$) used to reflect the asymmetry. In this equation, n is the mixing turbulent intensity. While n can vary depending on the turbulent flow condition, it is found for the symmetric flow condition as n = 5/6 (Guo *et al.* 2017). The shear velocity at the river bed can be calculated using all available data points as:

$$u_{\rm b}^{\star} = \frac{\Sigma_i \phi(\eta_{\rm i}, \lambda)(u_{\rm i} - u_{\rm c})}{\Sigma_{\rm i} \phi^2(\eta_{\rm i}, \lambda)}$$
(14)

The shear stresses can be computed as:

$$\tau_{\rm b} = \rho (u_{\rm b}^{\star})^2 \tag{15}$$

$$u_{\mathbf{i}}^{\star} = u_{\mathbf{b}}^{\star} \lambda \tag{16}$$

$$\tau_{\rm i} = \rho(u_{\rm i}^{\star})^2 \tag{17}$$

where ρ is the density of water.

Secondary flow visualization

The classical Rozovskii method is used to visualize the secondary flow pattern (Lane *et al.* 2000). The Cartesian components of the velocity u_x (east), u_y (north) and u_z (up) are used to derive the secondary components. The primary and the secondary flow components u_p and u_s are computed using the

projections of the east and north components on the depth-averaged velocity vector at the vertical:

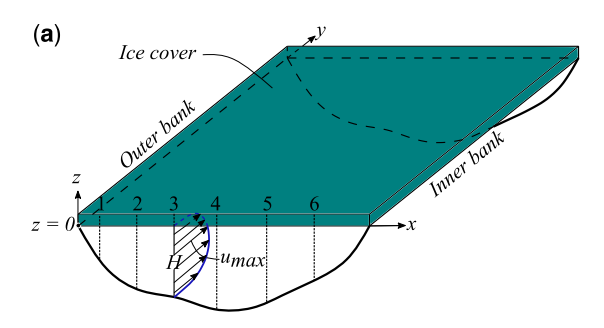
$$u_{\rm p} = (u_{\rm x}^2 + u_{\rm y}^2)^{0.5} \cos{(\theta - \omega)}$$
 (18)

$$u_{\rm s} = (u_{\rm x}^2 + u_{\rm y}^2)^{0.5} \sin{(\theta - \omega)}$$
 (19)

Here ω and θ are defined as the angle between the depth-averaged vector U and the time-averaged vector u to the x (east) direction in the counter-clockwise direction. The components $u_{\rm s}$ and the $u_{\rm z}$ are used to visualize the secondary flow pattern.

Theoretical model

To simplify the analysis, we introduced a local coordinate system (x, y, z), which changes from one cross-section to another. The x, y and z are the local cross-stream, streamwise and vertical direction,



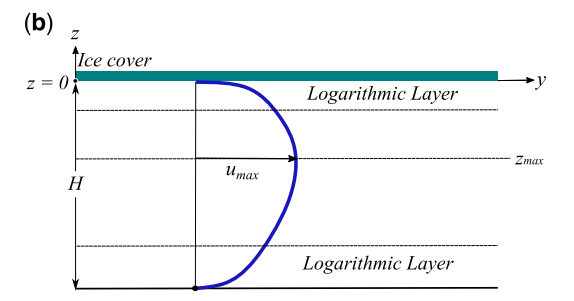


Fig. 3. (a) The mathematical model of the cross-stream momentum transfer utilizing the local coordinate system. (b) The vertical flow profile and the logarithmic layers under the ice cover. The ice—water interface is set at the level z=0. The main flow direction (streamwise) aligns towards the y axis. The cross-stream direction x starts from the outer bank x=0 towards the inner bank x=B. The local depth at one location on the cross-section defines the cross-sectional shape H(x). The maximum velocity u_{\max} appears near the mid-depth of the vertical under the ice cover. The verticals are numbered 1, 2, 3, etc. from the outer bank towards the inner bank across the cross-section. The number of verticals for each cross-section is shown in Table 1.

respectively. The cross-stream direction (x) is identified as the water–ice interface identically as shown in the model configuration in Figure 3. Here the coordinate system is local to each cross-section with x=0 at the intersection between the water surface and the outer bank. In the mathematical expressions, we assume a flat water–ice interface across the cross-sections. The ice–water interface is also used to determine the z=0 plane.

Three components of the velocity field $\vec{u}(u_1, u_2, u_3)$ are denoted as u_1, u_2 and u_3 in the x, y and z direction, respectively. Note that the streamwise velocity component is u_2 , whereas (u_1, u_3) are the cross-stream velocity components. Under this configuration, the distribution of the streamwise velocity profile $u_2(x, z)$ can be described by the balance of momentum (Devauchelle *et al.* 2022). The details of the mathematical analysis can be found in Appendix A.

With the use of turbulent viscosity v_t , the gravitational acceleration g, the energy slope S_f and ignoring the effect of curvature, the momentum equation reads:

$$v_{t} \left(\frac{\partial^{2} u_{2}}{\partial^{2} x} + \frac{\partial^{2} u_{2}}{\partial^{2} z} \right) + gS_{f} = 0$$
 (20)

The no-slip conditions on the ice—water interface and the river bed can be written as:

$$u_2 = 0$$
 for $z = 0$ (ice—water interface)
 $u_2 = 0$ for $z = -H(x)$ (river bed) (21)

Note that the flow depth H(x) changes from one vertical to the other (the cross-section shape) as shown in Figure 3. We assume that the river cross-section can be approximated by a polynomial function that is sufficiently smooth so that the side slope exists $\left(\frac{\partial H}{\partial x} \right) < \infty$ (Abramian *et al.* 2020).

By definition, the depth-averaged streamwise velocity (U_2) can be computed as:

$$\int_{z=-H}^{z=0} u_2 dz = U_2 H \tag{22}$$

Here we use the definition of the shear stresses on the ice (τ_i) and the bed (τ_b) surfaces:

$$\tau_{i} = \mu_{t} \frac{\partial u_{2}}{\partial z}|_{z=0}$$

$$\tau_{b} = \mu_{t} \frac{\partial u_{2}}{\partial z}|_{z=-H}$$
(23)

After several algebraic transformations as shown in Appendix A, equation (20) can be written as:

$$\rho v_{t} \frac{\partial^{2}}{\partial x^{2}} (U_{2}H) - \tau_{i}$$

$$- \tau_{b} \left(1 + \left(\frac{\partial H}{\partial x} \right)^{2} \right) + \rho g S_{f} H = 0$$
(24)

The impact of the lateral momentum transfer is accounted for by considering the variation of depth $(\partial H/\partial x)$ and the lateral transfer of turbulence $(\rho v_t \frac{\partial^2}{\partial x^2}(U_2H))$ along the cross-section. The ratio between the shear stresses can be related to the shear velocity ratio via a factor λ as follows:

$$\lambda = \frac{u_i^*}{u_k^*} \tag{25}$$

$$\frac{\tau_{\rm i}}{\tau_{\rm b}} = \frac{\rho(u_{\rm i}^{\star})^2}{\rho(u_{\rm b}^{\star})^2} = \lambda^2 \tag{26}$$

The bed shear stress can be estimated as:

$$\tau_{\rm b} = \frac{\rho g S_{\rm f} H + \rho v_{\rm t} (\partial^2 / \partial x^2) (U_2 H)}{1 + \lambda^2 (\partial H / \partial x)^2} \tag{27}$$

The value of depth-averaged v_t can be approximated as $v_t = 0.1u_b^*H$ (Vionnet *et al.* 2004). Once the bed shear stress (τ_b) is available from measurements, it is possible to validate our theoretical model by comparing the measured value of τ_b with the one obtained from equation (27). Accordingly,

the shear velocity can be estimated through the relationship of $u_b^{\bigstar} = \sqrt{\frac{\tau_b}{\rho}}$.

To validate the mathematical results with the measurement data, we introduce a notation ℓ to represent the measured distance from one point to the outer bank in the field measurements. Conceptually, ℓ and x are identical. However, it is challenging to determine the exact starting point of the cross-section under the ice cover. Thus, a reference point on the outer bank is selected for $\ell=0$. This selection does not affect all calculations since only the value of derivatives is needed in our model.

Results

Flow patterns induced by ice coverage

The statistical properties of the velocity time series u (z, t) are examined to determine the accuracy of the time-averaged $u_{\infty}(z)$ and the depth-averaged U_{∞} velocities. As illustrated in Figure 4, the values of the time-averaged velocity (u(z, T)) and depthaveraged velocity (U(T)) converge to the long-term values $(u_{\infty} \text{ and } U_{\infty})$ as the measurement duration T is increased. For example, the value of U(T) varies largely in the first 35 s of CS_3 -3. However, U(T)remains within 5% of U_{∞} as T < 35 s. The convergence of u(z, T) to u_{∞} at different depths exhibits a similar fashion for both CS₂-4 and CS₃-3. However, the impact of the ice surface and the river bed boundaries is evident. Measurement results show that the velocities at different depths in both stations including the one close to the surface (dashed blue line) and bed (dashed yellow line) are within 10% of the longterm values $(u_{\infty}(z))$ after the 40th second. Of note,

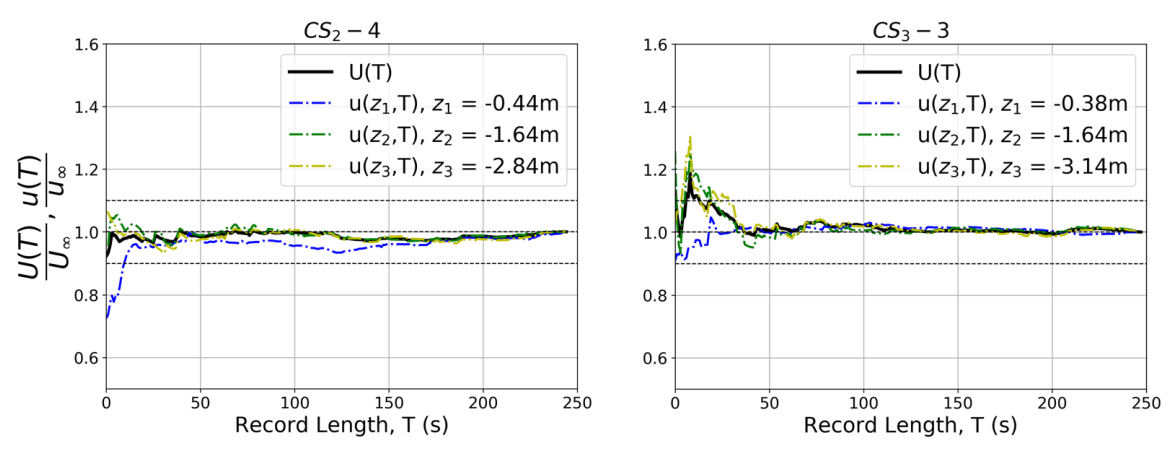


Fig. 4. The convergence properties (equation 2) of the time-averaged (u(z, T)) and depth-averaged (U(T)) velocities of CS₂-4 and CS₃-3 at different depths (z) as a function of the measurement duration T. The instantaneous velocity magnitude u(z, t) is computed from the east, north and up components of the measured ADCP data $u(z, t) = \sqrt{u_{\rm E}^2(z, t) + u_{\rm N}^2(z, t) + u_{\rm up}^2(z, t)}$. In both cases (the fourth station of CS₂ and the third station of CS₃), the measured verticals are located in the thalweg. The value of u(z, T) converges quickly within T = 100 s.

the velocity in the vicinity of the ice surface (z_1 =-0.44 m) at CS₂-4 fluctuates considerably until the 180th second. This type of fluctuation poses a challenge in obtaining accurate data near the ice cover.

As the value of U_{∞} is available for the ice holes, it is possible to reconstruct the flow pattern in the horizontal plane. The depth-averaged velocity vectors $(U_{\infty}(u_{\rm E}, u_{\rm N}))$ measured on 8 February 2022 are represented in Figures 5 and 6a. Here, the impact of the channel curvature can be seen clearly at crosssection CS₁, which is located next to the pedestrian bridge (see Fig. 2). The U vectors direct towards the inner (west) bank indicating a sharp turn in the large-scale flow pattern (see Figs 5 & 6a). On the other hand, the flow vectors in CS₂ show a spreading pattern, which is caused by the complex helical pattern at the bend apex. The flow adapts to the channel curvature well at CS₃ and CS₄. In comparison to the open-surface condition as seen in Figure 6b, the flow patterns at the corresponding cross-sections do not change significantly. While it is clear that the flow velocity is higher under the open-surface condition, the direction of the velocity vectors indicates a consistent flow planform. In brief, the presence of the ice cover did not alter significantly the flow planform in the bend.

The presence of the ice cover, however, altered the vertical flow profile completely. Figure 7 shows the measured vertical velocity profiles close to the outer bank ($\ell < 10 \, \text{m}$) under open-surface and ice-covered conditions. As shown in Figure 7a, the presence of a logarithmic layer can be found up to 1 m from the river bed under the open-surface condition (OS₂). As displayed at vertical CS₂-2

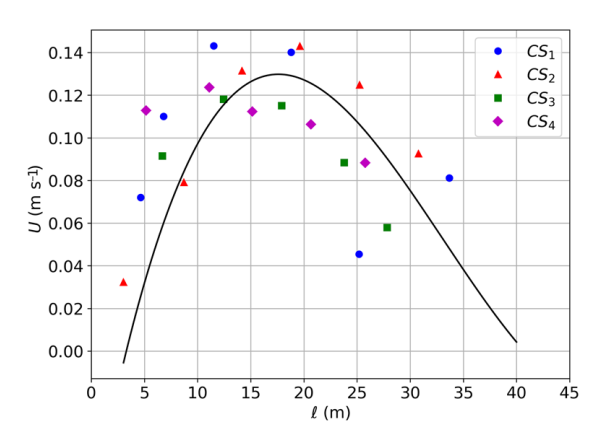


Fig. 5. The depth-averaged velocity profile U(x) in the river reach for the February 2022 measurement. The symbols represent the actual measurements at CS₁, CS₂, CS₃ and CS₄. The line denotes the assembled profile from the measured data as a guide for the eye. The assembled profile shows a slight asymmetry towards the outer bank. The distance to the outer bank ℓ is used as the cross-stream direction x (see also the diagram in Fig. 3).

(Fig. 7b), the ice cover changes the velocity profile into a nearly symmetrical shape owing to its additional resistance at the top. Moreover, the flow velocity under the ice cover is remarkably slower in comparison to the case under the open-surface condition (OS₂; Fig. 7a). In contrast to the open-surface condition, the logarithmic layer is not guaranteed to be found under the ice-covered condition. According to our logarithmic fitting methodology, the presence of the logarithmic layer is confirmed near the river bed for CS₂-2 as shown in Figure 7b ($R_{\rm bed}^2 = 0.96 > 0.70$). However, the logarithmic layer is not confirmed for the ice layer ($R_{\rm ice}^2 = 0.68 < 0.70$). The two-layer hypothesis is not considered valid for this case.

To evaluate the changes of the vertical velocity profiles along the river reach, the vertical profiles along the thalweg are plotted as seen in Figure 8. The presence of the ice cover shifts the position of the maximum time-averaged velocity (u_{max}) towards the river bed. As shown in Figure 8, the location of u_{max} is not close to the ice layer. In most cases, u_{max} is located at nearly one-half of the entire depth. The flow profiles vary from CS₁ to CS₄ along the thalweg. The value of $u_{\text{max}} \approx 0.15 \text{ m s}^{-1}$ and c. 0.12 m s⁻¹ at CS₁-3/CS₂-4 and CS₃-2/ CS_4 -1, respectively. The position of u_{max} at CS_1 -3 is around the mid-depth (z = -1.5 m); however, it is closer to the ice cover at the other three stations. Therefore, the channel curvature does have an effect in altering the position of the maximum core velocity in the vertical direction.

Logarithmic velocity profile

Logarithmic fitting is employed to determine the shear velocities as summarized in Table 2. The logarithmic layer is found only in certain verticals. In general, the logarithmic layer is evident if the flow depth is greater than 2 m. Two vertical profiles (CS_2 -6 and CS_3 -1) are presented in Figure 9a and b to demonstrate the extension of the logarithmic law in the ice layer. In the bed layer, the fitting is successful for 14 out of 22 verticals. It is important to note that the logarithmic layer can extend far (c. 1 m) from the ice and bed surface as shown in Figure 7. The details of the fitting are as follows.

The extension of the logarithmic layer in the bed layer is illustrated in Figure 9c (CS₁-3) and Figure 9d (CS₁-4). Here, $(H-|z|)^+$ is the dimensionless length representing the vertical distance from the channel bed. The separation from the logarithmic layer starts at $(H-|z|)^+ \approx 7000$ for the case CS₁-3, and $(H-|z|)^+ \approx 6500$ for the case CS₁-4. Thus, the extension of the logarithmic layer varies from one vertical to another.

The cross-stream distribution of u_b^* in CS₁, CS₂, CS₃ and CS₄ shows an increase in u_b^* near the banks

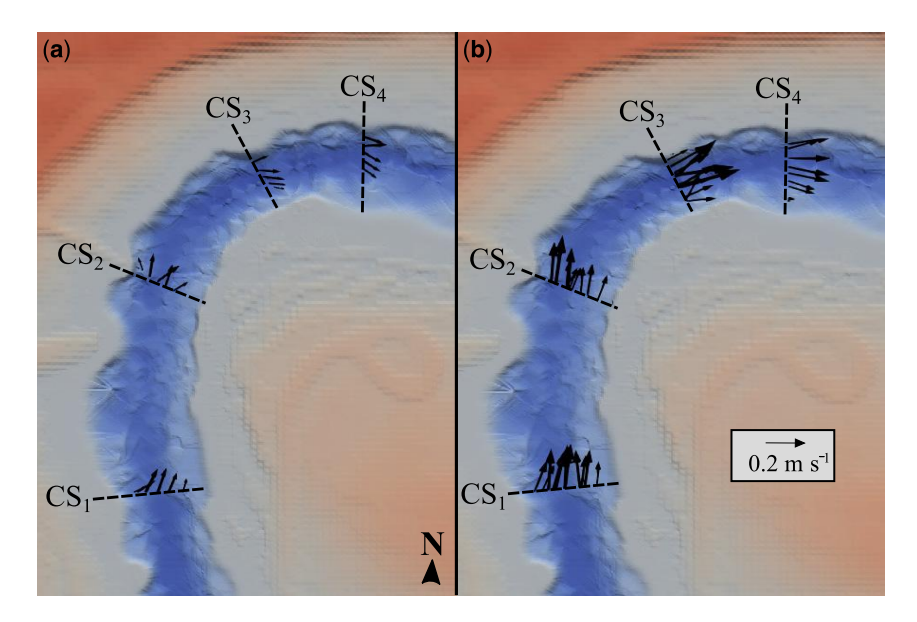


Fig. 6. Depth-averaged velocity (U) direction (a) under ice-covered conditions (8 February 2022), and (b) under open-surface conditions (10 October 2020). The value of U is computed using equation (2) from the measured time series. There exists a significant impact of the local bathymetry on the depth-averaged velocity distribution in addition to the channel curvature effect.

as seen in Table 2 (see also Fig. 12). The maximum u_b^{\star} value around the channel centre is found to be 0.0129 m s⁻¹ (CS₂-3). A higher value of $u_b^{\star} \approx 0.0163$ m s⁻¹ is found near the outer bank (CS₄-1). The value of u_b^{\star} is c. 0.0112 m s⁻¹ near the inner bank (CS₂-5). In brief, the bed shear stress is found to be higher near both banks in comparison to the channel centre.

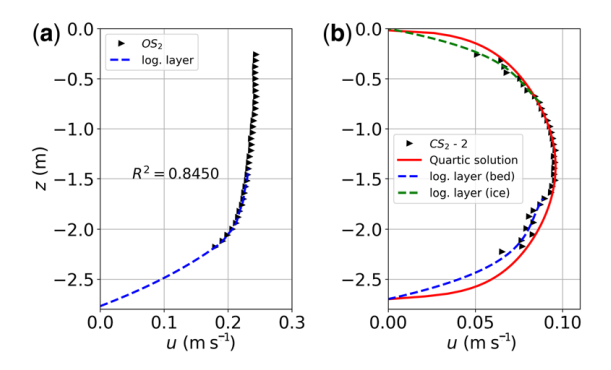


Fig. 7. The measured vertical velocity profiles near the outer bank at (a) station OS_2 ($\ell = 9.85$ m) on 2 October 2020 (open-surface conditions), and (b) station CS_2 -2 ($\ell = 8.75$ m) on 8 February 2022 (ice-covered conditions). Two separate values of R^2 were obtained during the fitting for the logarithmic layers: (i) near the ice (green dashed line) $R^2 = 0.68$; and (ii) near the bed (blue dashed line) $R^2 = 0.96$. The quartic solution (solid red line) is shown ($R^2 = 0.85$) to demonstrate its difference from the logarithmic profiles.

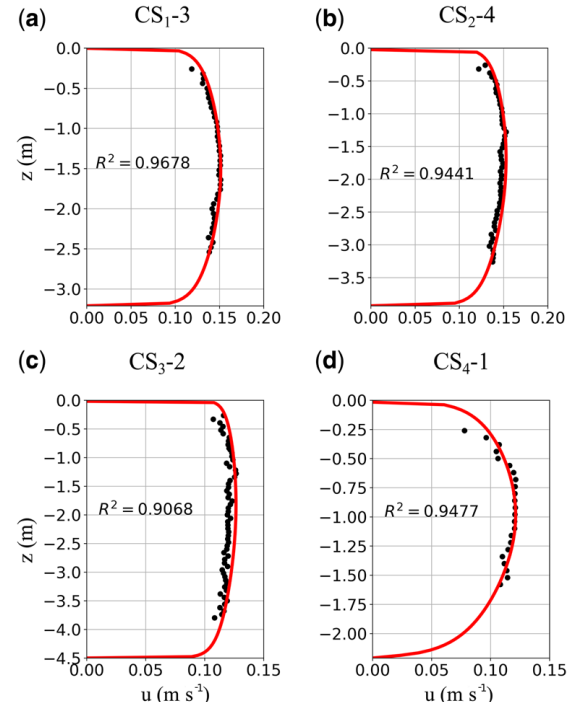


Fig. 8. The performance of the quartic solution in replicating the measured profiles along the vertical direction *z*. The measured vertical profiles (points) in ice holes of cross-sections CS₁-3, CS₂-4, CS₃-2 and CS₄-1 (see Fig. 6). The profiles are selected along the thalweg CS₁-3, CS₂-4, CS₃-2 and CS₄-1. The quartic profile (thick red line) is found by fitting equation (13) with the measured data. The parameters for the fitting of each ice hole are shown in Table 3.

Table 2. Derivation of the shear velocity u_i^* and u_b^* using the logarithmic fitting for the cases CS_1 , CS_2 , CS_3 and CS_4 (see Table 1)

| Case | H(m) | ℓ (m) | R^2 (bed) | u_b^{\bigstar} (m s ⁻¹) | R^2 (ice) | u_i^{\bigstar} (m s ⁻¹) |
|--------------------|------|------------|-------------|---------------------------------------|-------------|---------------------------------------|
| CS ₁ -1 | 1.10 | 4.66 | _ | _ | _ | _ |
| CS_1-2 | 2.35 | 6.83 | 0.7523 | 0.0075 | _ | _ |
| CS_1-3 | 3.21 | 11.58 | 0.9575 | 0.0066 | _ | _ |
| CS_1-4 | 3.55 | 18.90 | 0.9660 | 0.0062 | _ | _ |
| CS_1^{-5} | 3.23 | 25.30 | 0.8778 | 0.0060 | 0.7938 | 0.0021 |
| $CS_1^{-}6$ | 1.05 | 33.83 | _ | _ | _ | _ |
| CS_2^{-1} | 0.80 | 3.05 | _ | _ | _ | _ |
| CS_2^2 -2 | 2.70 | 8.75 | 0.9683 | 0.0121 | _ | _ |
| CS_2^2 -3 | 3.80 | 14.23 | 0.9202 | 0.0129 | _ | _ |
| CS_2^2-4 | 3.93 | 19.72 | 0.9000 | 0.0060 | 0.7831 | 0.0028 |
| CS_2^2-5 | 3.38 | 25.36 | 0.9526 | 0.0112 | _ | _ |
| CS_2^2 -6 | 2.40 | 30.91 | _ | _ | 0.9713 | 0.0112 |
| CS_3^2-1 | 2.40 | 6.70 | 0.9420 | 0.0135 | 0.8865 | 0.0031 |
| CS_3-2 | 4.50 | 12.50 | 0.7443 | 0.0035 | _ | _ |
| CS_3-3 | 4.41 | 17.98 | _ | _ | _ | _ |
| CS_3-4 | 3.95 | 23.59 | _ | _ | _ | _ |
| CS_3-5 | 3.23 | 27.71 | 0.9310 | 0.0107 | _ | _ |
| CS_4 -1 | 2.21 | 5.18 | 0.8841 | 0.0163 | 0.9622 | 0.0034 |
| CS_4 -2 | 3.64 | 11.16 | 0.8477 | 0.0060 | _ | _ |
| CS_4 -3 | 4.24 | 15.21 | _ | _ | _ | _ |
| CS ₄ -4 | 3.90 | 20.76 | 0.7495 | 0.0063 | _ | _ |
| CS_4 -5 | 3.34 | 25.88 | _ | _ | _ | _ |

The notation – denotes an unsuccessful fitting in that vertical. H and ℓ are the flow depth and the distance to the outer bank, respectively. The value of R^2 denotes the degree of fit.

Quartic profiles

The application of the quartic profile on ice-covered datasets suggests that it is applicable for most of the observed vertical profiles. Figure 8 illustrates the velocity distribution function (equation 13) of CS_1 -3, CS_2 -4, CS_3 -2 and CS_4 -1. The quartic solution is highly robust when the flow depth is sufficiently large (H < 2 m) as shown in Table 3. The R^2 value is mostly higher than 0.9 as shown in Table 3. Here, the position of u_{max} does not usually correspond to the symmetry plane $(\eta_{\text{max}} \neq 1)$. Our results confirm that the value of λ is generally less than 1 as shown in Table 3 in most verticals. These results imply that the location of u_{max} in most of the stations is closer to the ice surface (see equation 10). Exceptions are found in the verticals CS₁-2 and CS_4 -5 (near the banks) in which u_{max} is closer to the channel bed. In brief, the quartic method is robust in replicating the vertical profiles under ice cover.

The ability of the quartic profile to determine values of u_b^{\bigstar} using the velocity distribution function $(\phi(\eta,\lambda))$ in equation (14) is shown in Table 3. Comparing Tables 2 and 3, it is evident that the quartic velocity distribution provides significantly lower values for u_b^{\bigstar} . For example, the logarithmic method predicted $u_b^{\bigstar}=0.0060~\mathrm{m~s^{-1}}$ (Table 2) at CS₁-5. On the contrary, the quartic method gave $u_b^{\bigstar}=0.0037~\mathrm{m~s^{-1}}$ (Table 3) at the same vertical. In

conclusion, the quartic method provides a lower value for u_h^{\bigstar} .

Secondary flow patterns

The secondary flow pattern along the river reach is illustrated in Figure 10 using the classical rotationbased Rozovskii method. The overall pattern is convoluted, indicating the significant impact of the local bathymetry. At the first cross-section CS₁ there exists a strong return flow from the outer bank towards the thalweg at vertical 1. This return flow persists until the second cross-section CS₂. Additionally, two circulations are found near the verticals 3 and 5, which are closer to the banks. These single circulations are also present in other cross-sections CS₂, CS₃ and CS₄. Strikingly, double helical cells are observed in the second and third cross-sections (CS₂ and CS₃). At the verticals CS₂-4 and CS₃-4, counter-clockwise circulations are found both near the ice cover and the channel bed.

Modelling lateral momentum transfer

Equation (27) provides a reasonable estimation of lateral momentum transfer but it requires the evaluation of cross-stream derivatives. As shown in Table 1, the flow depth and velocities are obtained

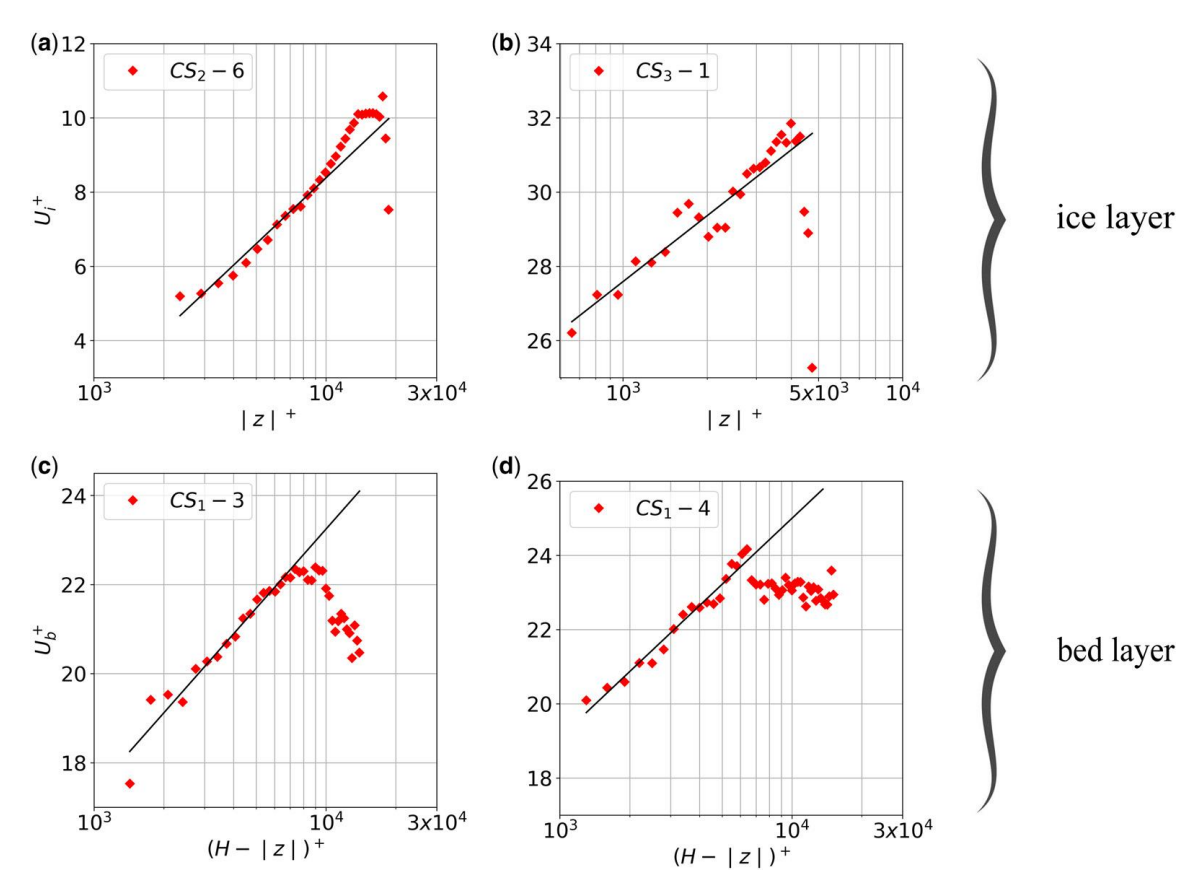


Fig. 9. The logarithmic fitting for the flow profiles near the (\mathbf{a}, \mathbf{b}) ice and (\mathbf{c}, \mathbf{d}) river bed surfaces. The absolute value of z (|z|) denotes the distance to the ice—water interface as shown in Figure 3. H is the total depth at the vertical. The cross-sections CS_1 , CS_2 , CS_3 and CS_4 are shown in Figure 2. The solid line denotes the logarithmic law of equation (3). The detailed parameters for the fitting in each ice hole are shown in Table 2.

only in several verticals. Therefore, there are insufficient data to generate estimations of these derivatives. Thus, a polynomial least-square method using a quadratic function $(f(x) = c_0 + c_1x + c_2x^2)$

is used to develop the fitting curve for the available datasets of H(x) and $U_2H(x)$. As an example, the cross-section profile of CS_2 is represented in Figure 11a. Our fitting results show excellent

Table 3. Derivation of the shear velocity on the bed layer (u_b^*) and on the ice layer (u_i^*) using the quartic solution for CS_1 , CS_2 , CS_3 and CS_4

| Case | $H\left(\mathbf{m}\right)$ | $u_{\rm max}$ | R^2 | $u_{\rm b}^{\bigstar}$ (m s ⁻¹) | u_i^{\bigstar} (m s ⁻¹) | λ | $\eta_{ m max}$ |
|--------------------|-----------------------------|---------------|--------|---|---------------------------------------|--------|-----------------|
| CS_1-2 | 2.35 | 0.1242 | 0.7663 | 0.0031 | 0.0047 | 1.5226 | 0.6027 |
| CS_1-3 | 3.21 | 0.1514 | 0.9678 | 0.0049 | 0.0050 | 1.0232 | 0.9771 |
| CS_1-4 | 3.55 | 0.1488 | 0.9409 | 0.0031 | 0.0023 | 0.7434 | 1.2881 |
| CS_1-5 | 3.23 | 0.1266 | 0.9563 | 0.0037 | 0.0031 | 0.8479 | 1.1635 |
| CS_2-2 | 2.70 | 0.0960 | 0.8470 | 0.0075 | 0.0067 | 0.9035 | 1.1011 |
| CS_2^- 3 | 3.80 | 0.1402 | 0.9061 | 0.0067 | 0.0049 | 0.7391 | 1.2935 |
| CS_2^- -4 | 3.93 | 0.1528 | 0.9441 | 0.0051 | 0.0036 | 0.6991 | 1.3434 |
| CS_{3}^{-1} | 2.40 | 0.0991 | 0.9150 | 0.0044 | 0.0024 | 0.5482 | 1.5379 |
| CS_3-2 | 4.50 | 0.1265 | 0.9068 | 0.0031 | 0.0019 | 0.6256 | 1.4374 |
| CS_4-1 | 2.21 | 0.1211 | 0.9477 | 0.0087 | 0.0058 | 0.6714 | 1.3786 |
| CS_4-4 | 3.90 | 0.1098 | 0.9372 | 0.0017 | 0.0008 | 0.4586 | 1.6525 |
| CS ₄ -5 | 3.34 | 0.0956 | 0.9099 | 0.0008 | 0.0016 | 1.9778 | 0.4072 |

The position of η_{max} and the value of u_{max} are determined by optimizing the R^2 of the velocity distribution function. The details of the mathematical notations are explained in equations (10–14).

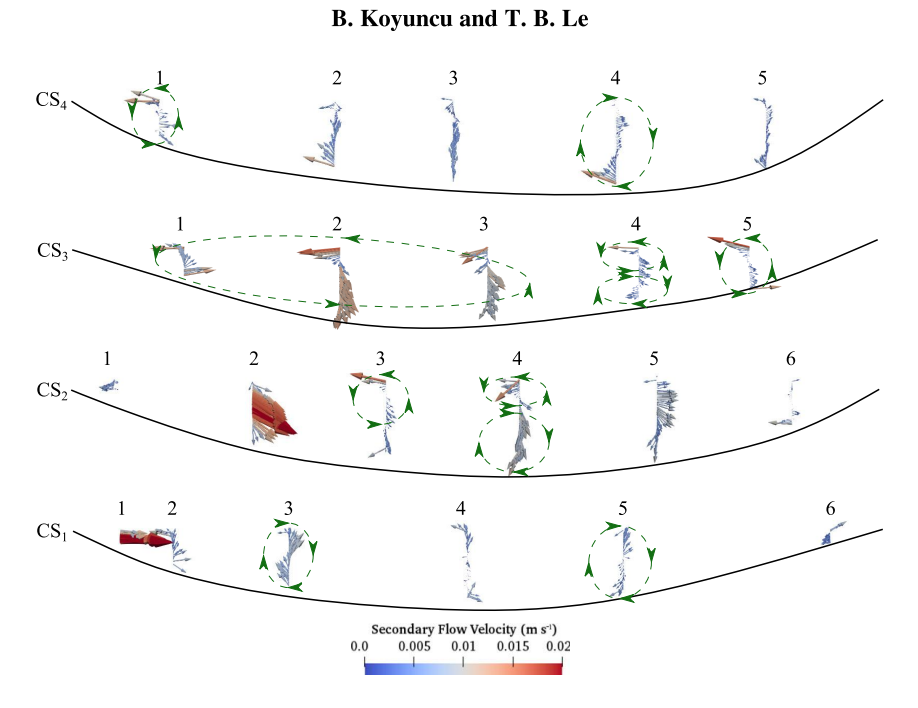


Fig. 10. The secondary flow pattern is visualized by the classical Rozovskii method (Lane *et al.* 2000). The secondary flow velocity pattern changes from one cross-section to another as the helical cells emerge. The double-stacked cells are found at the cross-sections CS_2 and CS_3 . Flow direction follows the north direction (from bottom to top).

agreements between the measured data and the quadratic curves with $R^2 > 0.75$. The shape of the cross-section can be described reasonably well by the fitted curve. However, the precise location of the thalweg is slightly shifted towards the inner bank. The unit flow rate $(U_2H(x))$ is also well captured by the fitting process as depicted in Figure 11b. The values of $(\partial H(x)/\partial x)$ and $(\partial^2(U_2H)/\partial x)$

(x))/ ∂x^2) are derived from the coefficients c_0 , c_1 and c_2 of the fitted curve.

Manning's formula is used to estimate the energy slope (S_f) from the mean velocity V = Q/A with the flow discharge Q and the cross-sectional area A as:

$$S_{\rm f} = \frac{(V_n)^2}{R_{\rm h}^{4/3}} \tag{28}$$

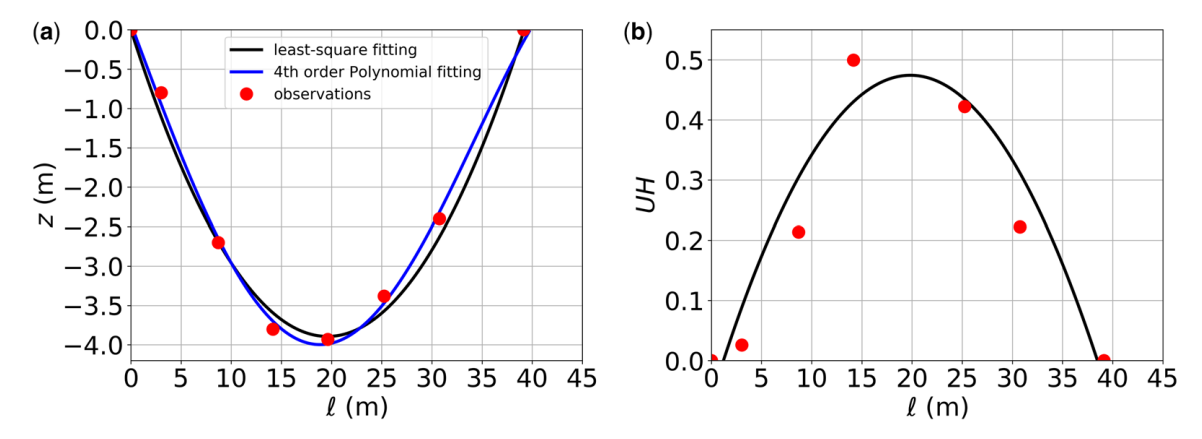


Fig. 11. Procedures to compute the cross-stream derivatives. The least-square fitting is performed for: (a) the water depth (H(x)), the cross-sectional shape); and (b) the unit flow rate q(x) = U(x)H(x). The depth and the unit flow rate of the cross-section CS_2 are shown as an illustration of the procedure. The quadratic polynomial $f(x) = c_0 + c_1 x + c_2 x^2$ is used as the trend line. The fitting procedure is carried out using the least-square fitting to determine c_0 , c_1 and c_2 . The derivatives $(\partial H/\partial x)$ and $(\partial^2 (UH)/\partial x^2)$ are evaluated by differentiating the function f(x). Note that the measured distance to the outer bank ℓ is used as the cross-stream direction x.

Here the hydraulic radius (R_h) and the roughness coefficient n are computed as follows.

A one-dimensional HEC-RAS model is developed for the river reach to determine $R_{\rm h}$ and n using the DTM in Figure 2. The rating curve (Q, H) at the USGS Fargo (09020104) station is used to calibrate the value of Manning's n under the open-surface condition. The roughness coefficient is estimated for the bankfull condition as $n \approx 0.0166$. Accordingly, the average energy slope for the entire river reach is estimated as $S_{\rm f} = 6.9 \times 10^{-6}$. The depth-averaged eddy viscosity $v_{\rm t}$ is estimated as $v_{\rm t} = 10^{-6}$ m² s⁻¹ (Vionnet *et al.* 2004).

The validity of the theoretical model is tested in the cross-sections CS₁, CS₂, CS₃ and CS₄ as shown in Figure 12. The theoretical value of u_b^{\bigstar} is calculated using equation (27) and the guided value of λ in the range from 0.45 to 2.0, which is observed in Table 3. At the channel centre from CS₁ to CS₄, the theoretical model predicts well the variation of $u_{\rm b}^{\star}$ given the bounds of λ . The model captures well the upper and lower bounds of u_b^* and their trends as evident in Figure 12. In particular, the proposed theory is able to capture the elevated values of $u_{\rm b}^{\star}$ $(0.0150 \text{ m s}^{-1})$ and the lowest values ($\approx 0.005 \text{ m}$ s^{-1}). The impact of the channel curvature can be seen as the magnitude of the measured shear velocity is significantly larger near the outer bank. The theoretical model fails to capture this feature. The model significantly underpredicts $u_{\rm b}^{\star}$ near the outer bank $(CS_3-1 \text{ and } CS_4-1).$

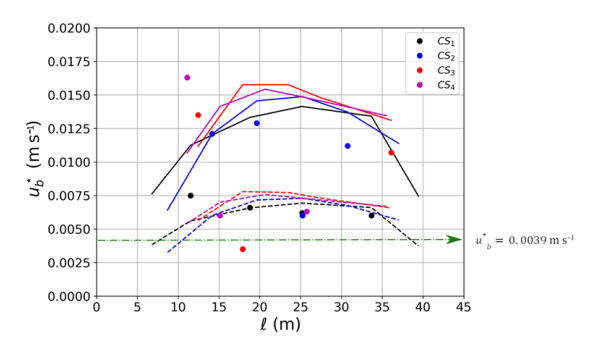


Fig. 12. The comparison between the cross-stream momentum model (equation 27) and the measured cross-stream shear velocity profile in the river reach. The bed shear velocity (u_b^{\star}) is computed from the logarithmic fitting for the cross-sections CS_1 , CS_2 , CS_3 and CS_4 (see Table 2). The predicted values are generated using two different values of λ (equation 27 and $u_b^{\star} = \sqrt{\frac{\tau_b}{\rho}}$) for each cross-section: (i) $\lambda_{\min} = 0.45$ (solid lines); and (ii) $\lambda_{\max} = 2.0$ (dashed lines). The range of λ is selected from the quartic solution fitting of the measurements (Table 3). The value of u_b^{\star} (green dash–dotted line) is calculated with $u_b^{\star} = V\sqrt{\frac{f}{8}}$ (see equation 29).

Discussion

Cross-stream momentum transfer plays an important role in regulating the river width via the modulation of sediment flux (Abramian et al. 2020). The sediment transport is balanced out in the bank region under the equilibrium condition where the gravity force and the bed shear stress equate to each other (Phillips and Jerolmack 2016; Popović et al. 2021). In ice-covered rivers, the roughness of the ice layer adds further complexities by introducing the shear stress in the ice layer (τ_i) and altering the one in the bed layer (τ_b) (Guo et al. 2017). Most previous works have not considered the impact of ice cover on the cross-stream momentum transfer. Our work develops a framework to investigate the cross-stream distribution of τ_i and τ_b , which is important in regulating the morphology of rivers in cold regions (Gautier et al. 2021).

Impacts of ice cover on the vertical profiles

The two-layer hypothesis (see also Fig. 3) assumes the presence of two logarithmic profiles near the bed and ice layers concurrently (Sukhodolov et al. 1999). This has been the main approach to describing vertical velocity distribution in many previous studies (Urroz and Ettema 1994; Attar and Li 2012, 2013). Since the applicability of the logarithmic method is based on the availability of the data near the surface, the problem of signal interference is critically important. As our previous work indicated, obtaining flow data under the ice-covered condition is challenging owing to signal interference near both boundaries (see also Fig. 4) (Koyuncu and Le 2022). This challenge dictates the logarithmic fitting for both the ice and the bed layers at the same vertical. As illustrated in Table 2, there are only a few verticals where both logarithmic layers are recognized (CS₁-5, CS₂-4, CS₂-6, CS₃-1 and CS₄-1). The reason for this challenge can be further investigated in the wall units (z^+, u^+) . As shown in Figure 9a and b, the first available point is located for logarithmic fitting around $|z|^+ = 1100$ in the wall units. The last available point is typically less than $|z|^+ = 5000$, which is approximately less than 20% of the total depth (H). The logarithmic fitting requires a sufficient number of data points to fall into this range of $1100 < |z|^+ < 5000$ (Petrie and Diplas 2016). In practice, this requirement prohibits an acceptable fitting in many verticals as demonstrated in Table 2. Therefore, the logarithmic fitting is not a robust method to determine u_i^* and u_h^* .

In addition to the data requirement, the main limitation of the two-layer hypothesis is that it introduces a discontinuous velocity gradient at the location of u_{max} . As shown in Figure 7, the two-layer hypothesis cannot capture the entire profile because

the two logarithmic profiles do not intersect at the maximum velocity location. The quartic profile is introduced to alleviate this shortcoming via the use of all velocity data in the mixing core (mid-depth) as depicted in Figure 7b (Guo *et al.* 2017). The quartic profile provides an excellent model for the ice-covered flows as shown in Figure 8 at all ice holes. Despite the missing data near the river bed layer (\approx 0.5 m), the quartic profile can follow the measured data closely with $R^2 > 0.90$ in most cases (see Table 3). This is remarkable given that the quartic profile needs a minimal number of fitting parameters such as λ and α .

The impact of banks on the vertical profile is evident as shown in Figure 8. Field measurement has demonstrated the impact of banks on altering the vertical profiles under the open-surface condition (Chauvet et al. 2014). A similar phenomenon is observed in this study since the profiles are altered as they are closer to the banks. Near the thalweg (CS₁-3, CS₂-4), the profiles are nearly symmetrical. Near the banks, the location of u_{max} is closer to the ice layer. As shown in the Table 3, the value of $\lambda = (u_i^*/u_h^*)$ varies significantly from one vertical to another. As shown in Table 3, the value of λ is typically less than 1.0 in the thalweg region but it can reach 2.0 in the bank region. Hence, the bank has a critical role in regulating the vertical profile and the shear stresses.

Three-dimensional structures of flow in ice-covered bends

To date, our understanding of ice-covered flows in rivers has been rather limited (Lotsari et al. 2017). Most of the previous work has been carried out in laboratory conditions (Urroz and Ettema 1994; Ettema 2002; Wang et al. 2020). There are a limited number of field measurements for small ice-covered rivers (Sukhodolov et al. 1999; Demers et al. 2011; Lotsari et al. 2017). The most prominent feature of ice-covered flows in bends is found in laboratory conditions in which the vertical profiles possess two points of inflexion (Urroz and Ettema 1994; Tsai and Ettema 1996). Field measurement by Urroz and Ettema (1994) confirms that this feature indeed exists in a natural bend meander as 'doublestacked vortices' (Demers et al. 2011). The laboratory experiment by Urroz and Ettema (1994) suggests that the flow structures consist of two counter-rotating circulations as opposed to a single one in the open-surface condition. The field measurement of Demers et al. (2011) further clarifies that the spatial extent of these double-stacked vortices is limited in the bend apex. Field data by Lotsari et al. (2017) confirm that the presence of the doublestacked vortices is sensitive to the water depth since these vortices disappear under low flow conditions. Similar field measurements have not been carried out for medium-sized and large rivers to investigate the structure of these vortices.

From the measurements of secondary flows in Figure 10, it is possible to reconstruct the three-dimensional structure of the ice-covered flow in the studied bend as shown in Figure 13. In general, the flow consists of longitudinal circulations that rotate in the opposite direction to each other. Two helical circulations are found near the banks in addition to a counter-clockwise rotation in the thalweg. Near the bend apex, the double-stacked vortices appear intermittently between CS_2 and CS_3 . The double-stacked vortices seem to merge at CS_4 as the flow exits the bend. In brief, the three-dimensional flow structures are organized as separate helical flows and they interact with each other along the bend.

In general, our three-dimensional flow model agrees well with the field observations of Demers *et al.* (2011) and Lotsari *et al.* (2017). As shown in Figures 6, 7 and 9, the ice cover directs the high-velocity core towards the outer bend and the middepth at the same time, as reported in Demers *et al.* (2011). In addition, the intermittent presence of the double-stacked vortices near the bend apex is almost identical to the one in the observations of Demers *et al.* (2011) and Lotsari *et al.* (2017). Interestingly, our results also confirm the transition of the double-stacked vortices towards a single vortex structure at the bend downstream end (Demers *et al.* 2011).

Our field data further indicate that the threedimensional flow structures are more complicated than those predicted by the model of Lotsari *et al.* (2017). In addition to the main circulation in the thalweg, there exist two additional circulations near

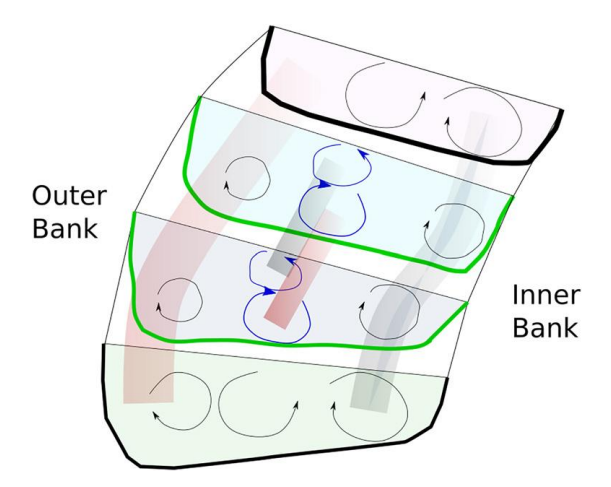


Fig. 13. The hypothesized three-dimensional structure of the flow in the ice-covered bend. Two clockwise rotations are located near the outer and inner banks, respectively. The double-stacked vortices appear near the bend apex.

the banks. Note that the presence of multiple circulations in one cross-section has been reported in previous field measurements (Chauvet et al. 2014). Here the thalweg circulation is the classical secondary flow, which is driven by the channel curvature. However, the other circulations are driven by turbulence anisotropy (Kang and Sotiropoulos 2011). Owing to the three-dimensional structure of the flow, it is challenging to capture the dynamics of these vortices at all cross-sections as shown in Figure 10 as it requires the period of measurement (T) to be sufficiently large. In previous works, the presence of bank vortices has not been reported (Demers et al. 2011; Lotsari et al. 2017). The absence of bank vortices in these studies might also be due to the difference in the stream depth. The measurements of Lotsari et al. (2017) and Demers et al. (2011) were carried out for shallow bends (c. 1.5-2 m), whereas the maximum depth of the current bend is c. 4 m, which is significantly deeper. Thus, both the flow depth and the bend curvature could play important roles in regulating the emergence of helical motions in ice-covered bends (Lotsari et al. 2017). We hypothesize that the double-stacked vortices only appear in regions where the flow depth reaches a critical threshold.

The cross-stream momentum equation

The traditional approach in river hydraulics considers only the ice-free condition and ignores the bank effects (e.g. $u_b^{\star} \approx \sqrt{gHS}$) (Phillips and Jerolmack 2016). In order to provide a similar method to estimate the numerical value of u_b^{\star} under ice cover, we propose the use of the Haaland's equation (friction method) for a closed duct as:

$$\frac{1}{\sqrt{f}} = -1.8 \log \left[\left(\frac{\frac{2.95 d_{84}}{4R_{\rm h}}}{3.7} \right)^{1.11} + \frac{6.9}{\text{Re}} \right]$$
 (29)

where Re, R_h and f are the Reynolds number $(Re = (V(4R_h)/\mu))$, the hydraulic radius and the friction coefficient, respectively. Here $d_{84} = 0.00288$ m is the sediment particle size of the Red River in Fargo (Galloway and Nustad 2012). Following the computation of f, the shear velocity near the channel bed is

calculated $(u_b^* = V\sqrt{\frac{f}{8}})$ and represented in Figure 12 (Finnemore and Franzini 2002). Using this formula, the estimated u_b^* value is computed as 0.0039 m s⁻¹. As seen in Figure 12, this value is in the range of our field observation (lower bound), which generally agrees with the estimated values from the quartic solution (see Table 3). However, this is a single value

for the entire cross-section and thus the cross-stream distribution of the bed shear stress cannot be generated.

In contrast to the above-mentioned approach, equation (27) shows that the presence of the ice cover complicates the bed shear stress distribution by introducing the effect of bank slope, the local flow turbulence and the distortion of the vertical profile (λ) . Thus, equation (27) can be used to estimate the bed shear stress under the ice-covered condition in any location in the cross-section.

The significant contribution of equation (27) is that it also establishes the linkage between τ_i and $\tau_{\rm b}$. It is an alternative method to compute $\tau_{\rm i}$ as long as the value of τ_b is available via either the logarithmic or quartic method. In addition, the roles of the cross-section shape H(x) and the unit flow rate profile $U_2H(x)$ are evident in the bed shear stress distribution (see Fig. 11). The presence of the bank slope dictates the bed shear stress via the term $(\partial H/\partial x)$. The cross-sectional flow profile $(U_2(x))$ plays a role in distributing the momentum via turbulent stress. Therefore, these terms become significant in regulating the bed shear stress near banks where their gradients are large. These effects can be observed as the value of $u_{\rm b}^{\star}$ is elevated near the banks, as evident in Table 3.

To test the sensitivity of the u_b^{\dagger} calculation to the choice of the representation of H(x), a fourth degree polynomial is also used to fit the geometrical form of H(x) (see Fig. 11a). Our results show that the fourth degree polynomial does not provide significant improvements in terms of capturing the location of the thalweg. Therefore, our results indicate that a second order polynomial is sufficient to capture the geometrical shape of the cross-sections in the current study.

Note that the cross-stream momentum (equation 39) is a simple model that relates the shear stresses on the bed and the ice cover layers. Therefore, our model for lateral momentum transfer has several limitations. First, we assume that the channel curvature has no effect since the variation of the streamwise component of the velocity has been ignored, (∂u) $\partial y = 0$. Natural rivers often follow a meandering path that changes the entire flow structure by shifting the position of the main flow and thalweg towards the outer bank. This pattern generates a high-shearstress region near the outer bank (Koyuncu and Le 2022). Indeed, the skewed distribution depth-averaged velocity U(x) is observed in the cross-sections CS₁, CS₂, CS₃ and CS₄ (Fig. 6). This skewed distribution affects the ability of the model to capture the bed shear stress near the outer bank in cross-sections CS₃ and CS₄ (see Fig. 12). Here, the model fails to capture the large bed shear stress near the outer bank at stations CS₃-1 and CS₄-1 owing to the sharp curvature of the channel.

Furthermore, our model assumes that the ice layer is completely flat across the cross-section $(\partial z_{\rm ice}/\partial x = 0)$ at z = 0). However, there could be a cross-stream slope between the surface elevation of the inner and outer banks (super-elevation effect in a meander bend). Thus, our equation (27) must be modified to account for such an effect. In addition, the number of ice holes in a cross-section must be increased to increase the accuracy of the fitting procedure for H(x) and UH(x) as seen in Figure 11. Nevertheless, the proposed model can provide a reasonable estimation in the range of u_b^{\bigstar} in the ice-covered reach using available inputs such as the energy slope S_f and the range of λ . Future efforts will be made to refine the assumptions to improve the estimation for τ_b .

Conclusions

We studied the three-dimensional structure of flows in an ice-covered bend. Field measurements were carried out to obtain flow velocity data in a river reach of the Red River, North Dakota, USA. Our study revealed the importance of ice coverage on the bed shear stress by regulating the velocity profile. Based on field data, we developed a mathematical model for the cross-stream momentum transfer in ice-covered rivers in general. Our model also emphasizes the importance of flow dynamics near banks as the flow profiles are altered significantly in shallow areas under ice coverage. As a result, the crosssectional distribution of the bed shear stress is highly dependent on the distance to the banks. Our theoretical model and field data show a significant increase in bed shear stress near both banks.

Our main conclusions are:

- It is challenging to apply the two-layer hypothesis to the study area. In most cases, the logarithmic layers are not observed at the same vertical using our fitting methodology.
- The quartic profile provides a robust method to estimate the bed shear stress under the ice-covered condition. However, the quartic profile underestimates the bed shear stress.
- We propose a simple formula to compute the cross-stream distribution of bed shear stress under ice-covered conditions. Using this formula and our field measurement data, we show that the bed shear stress is significantly affected by the ice cover, especially in the bank regions.
- Our field data show that the secondary flow pattern under the ice-covered condition might be more complicated than previously thought, with double-stacked vortices observed at the bend apex. Their locations agree with previous works (Demers et al. 2011; Lotsari et al. 2017). However, additional helical cells also exist as separate longitudinal structures along the river reach.

Acknowledgements We give special thanks to Dr Xuefeng Chu (NDSU) for initiating our interest in ice hydraulics. We acknowledge the assistance of Daniel Thomas (USGS) and the Dakota Water Science Centre in measuring and providing data for flows under the ice coverage. We would like to thank Peter Goettsch and Christopher Broz (USGS) for helping us to set up the measurement configuration. We also would like to thank reviewers for taking time to provide valuable comments and suggestions to enhance the quality of the manuscript.

Competing interests The authors declare that they have no known competing financial interests or personal relationships that could have appeared to influence the work reported in this paper.

Author contributions BK: formal analysis (lead), investigation (equal), methodology (equal), software (lead), validation (equal), visualization (lead), writing – original draft (equal), writing – review & editing (equal); TBL: conceptualization (lead), funding acquisition (lead), investigation (equal), methodology (equal), project administration (lead), resources (lead), supervision (lead), validation (equal), writing – original draft (equal), writing – review & editing (equal).

Funding This work is mainly supported by a start-up package of Trung Le from North Dakota State University (NDSU) and a grant from the North Dakota Established Program to Stimulate Competitive Research Office, award no. FAR0032223. In addition, Berkay Koyuncu is supported by predoctoral fellowships from the North Dakota Water Resources Research Institute and the Environmental Conservation Sciences programme of NDSU, and a fellowship from the United States Geological Survey. This work is also based on materials provided by the ESIP Lab with support from the National Aeronautics and Space Administration (NASA), National Oceanic and Atmospheric Administration (NOAA) and the United States Geological Survey (USGS). We also acknowledge the use of computational resources at the Centre for Computationally Assisted Science and Technology (CCAST)-NDSU and an allocation (CTS200012) from the Extreme Science and Engineering Discovery Environment (XSEDE), which is supported by National Science Foundation grant number ACI-1548562. We acknowledge the financial support of NSF RET – 1953102 to disseminate the findings of this study to local communities including K-12 teachers in the City of Fargo and West Fargo, North Dakota.

Data availability LiDAR data from the State Water Commission of North Dakota are available at https://lidar.dwr.nd.gov/. Our raw velocity data are available at https://github.com/trunglendsu/ESIP/tree/main/ADCP_Data and https://github.com/trunglendsu/ESIP/tree/main/Modeling-the-shear-stress-distribution-in-a-cross-sec tion-of-an-ice-covered-stream-main.

Appendix A

Our theoretical model is based on the lubrication approximation (Devauchelle *et al.* 2022). The following assumptions were made:

- The flow is steady. Unsteady effects are not accounted for.
- No curvature effect of the channel planform is considered (e.g. straight channel only).
- The top surface is completely covered by ice. No opensurface zones are observed on the top surface.
- The effects of bedform and ice scallops are not considered in the current model. The ice surface is considered to be flat ($z_{ice} = const$) and it has a grain-size roughness height of k_s (rough wall).
- The turbulent viscosity v_t is constant in the vertical direction.
- In the case of ice-covered flow, the situation is similar to flow in a pipe or a closed duct. Note that there are three different pressure gradients along three directions: $\partial p/\partial x$ (cross-stream direction), $\partial p/\partial y$ (stream direction) and $\partial p/\partial z$ (vertical direction). We ignore the cross-stream pressure gradient $\partial p/\partial x = 0$ as the river width $(B \approx 40 \text{ m})$ is much smaller than the river reach $(L \approx 1 \text{ km})$. The pressure gradient along the y direction $\partial p/\partial y$ drives the flow and it is implicitly included in the flow momentum balance (equation A10). We assume that the pressure gradient along the vertical direction $\partial p/\partial z$ follows a hydrostatic pressure law since it is a valid assumption for gravity-driven flows in closed ducts and pipes (Finnemore and Franzini 2002).

The details of the transformation for the momentum are as follows:

First, the momentum equation is written as:

$$v_{\rm t} \left(\frac{\partial^2 u_2}{\partial^2 x} + \frac{\partial^2 u_2}{\partial^2 z} \right) + gS_{\rm f} = 0$$
 (A1)

The no-slip conditions on the ice—water interface and the river bed can be written as:

$$u_2 = 0$$
 for $z = 0$ (ice—water interface)
 $u_2 = 0$ for $z = -H(x)$ (river bed) (A2)

Ignoring the channel curvature and revoking the fully developed flow condition (all the derivatives with respect to *y* are zero), the turbulent stresses read:

$$\tau_{x} = \tau_{xy} = \mu_{t} \left(\frac{\partial u_{2}}{\partial x} + \frac{\partial u_{1}}{\partial y} \right) = \mu_{t} \left(\frac{\partial u_{2}}{\partial x} \right)$$

$$\tau_{yy} = 0$$

$$\tau_{z} = \tau_{yz} = \mu_{t} \left(\frac{\partial u_{2}}{\partial z} + \frac{\partial u_{3}}{\partial y} \right) = \mu_{t} \left(\frac{\partial u_{2}}{\partial z} \right)$$
(A3)

Here $\mu_t = \rho v_t$ with ρ being water density. Now the momentum equation can be integrated along the depth in each vertical $(z = -H \rightarrow z = 0)$ assuming that v_t is invariant across the depth:

$$v_{t} \int_{z=-H}^{z=0} \frac{\partial^{2} u_{2}}{\partial^{2} x} dz + v_{t} \int_{z=-H}^{z=0} \frac{\partial^{2} u_{2}}{\partial^{2} z} dz + \int_{z=-H}^{z=0} g S_{f} dz = 0$$
 (A4)

Note that we can calculate the first integral using the Leibniz's rule:

$$\frac{\partial}{\partial x} \left(\int_{z=-H}^{z=0} \frac{\partial u_2}{\partial x} dz \right) = \frac{\partial u_2}{\partial x} |_{z=0} \frac{\partial z}{\partial x} |_{z=0} + \frac{\partial u}{\partial x} |_{z=-H} \left(\frac{\partial H}{\partial x} \right)_{z=-H} + \int_{z=-H}^{z=0} \frac{\partial^2 u_2}{\partial^2 x} dz$$

Here we assume that the ice-water interface is flat $\frac{\partial z_{\rm ice}}{\partial x}|_{z=0}=0$; this results in the relation:

$$\int_{z=-H}^{z=0} \frac{\partial^2 u_2}{\partial^2 x} dz = \frac{\partial}{\partial x} \left(\int_{z=-H}^{z=0} \frac{\partial u_2}{\partial x} dz \right) - \frac{\partial u_2}{\partial x} |_{z=-H} \frac{\partial H}{\partial x}$$

By the chain rule:

$$\frac{\partial u_2}{\partial x}|_{z=-H} = \frac{\partial u_2}{\partial z} \frac{\partial z}{\partial x}|_{z=-H} = -\frac{\partial u_2}{\partial z}|_{z=-H} \frac{\partial H}{\partial x}$$

Therefore, the momentum equation (equation A4) now becomes:

$$v_{t} \left(\frac{\partial}{\partial x} \left(\int_{z=-H}^{z=0} \frac{\partial u_{2}}{\partial x} dz \right) - \frac{\partial u_{2}}{\partial z} |_{z=-H} \left(\frac{\partial H}{\partial x} \right)^{2} \right) + v_{t} \frac{\partial u_{2}}{\partial z} |_{z=-H}^{z=0} + gS_{f}H = 0$$
(A5)

By definition, the depth-averaged streamwise velocity (U_2) can be computed as:

$$\int_{z=-H}^{z=0} u_2 dz = U_2 H$$

Now the Leibniz's rule gives:

$$\frac{\partial}{\partial x} \left(\int_{z=-H}^{z=0} u_2 dz \right) = \frac{\partial}{\partial x} (U_2 H)$$

$$= u_2|_{z=0} \frac{\partial z}{\partial x}|_{z=0} + u_2|_{z=-H} \frac{\partial H}{\partial x}$$

$$+ \int_{z=0}^{z=0} \frac{\partial u_2}{\partial x} dz$$
 (A6)

Note that we invoke the flat surface condition again, $\frac{\partial z_{\text{ice}}}{\partial x}|_{z=0} = 0$, and the no-slip condition $u|_{z=-H} = 0$, and we finally have:

$$\frac{\partial}{\partial x} \left(\int_{z=-H}^{z=0} u_2 dz \right) = \int_{z=-H}^{z=0} \frac{\partial u_2}{\partial x} dz$$
 (A7)

Now substitute equation (A7) into equation (A5):

$$v_{t} \left(\frac{\partial}{\partial x} \left(\frac{\partial (U_{2}H)}{\partial x} \right) - \frac{\partial u_{2}}{\partial x} |_{z=-H} \left(\frac{\partial H}{\partial x} \right)^{2} \right) - \tau_{i} - \tau_{b} + g S_{f} H = 0$$
(A8)

Here we use the definition of the shear stresses on the ice (τ_i) and the bed (τ_b) surfaces:

$$\tau_{i} = -\mu_{t} \frac{\partial u_{2}}{\partial z} |_{z=0}$$

$$\tau_{b} = \mu_{t} \frac{\partial u_{2}}{\partial z} |_{z=-H}$$
(A9)

or we can write:

$$\rho v_{t} \frac{\partial^{2}}{\partial x^{2}} (U_{2}H) - \tau_{i} - \tau_{b} \left(1 + \left(\frac{\partial H}{\partial x} \right)^{2} \right) + \rho g S_{f} H = 0$$
(A10)

References

- Abramian, A., Devauchelle, O. and Lajeunesse, E. 2020. Laboratory rivers adjust their shape to sediment transport. *Physical Review E*, **102**, 053101, https://doi.org/10.1103/PhysRevE.102.053101
- Attar, S. and Li, S.S. 2012. Data-fitted velocity profiles for ice-covered rivers. *Canadian Journal of Civil Engi*neering, 39, 334–338, https://doi.org/10.1139/ 12012-001
- Attar, S. and Li, S.S. 2013. Momentum, energy and drag coefficients for ice-covered rivers. *River Research and Applications*, **29**, 1267–1276, https://doi.org/10.1002/rra.2611
- Blanckaert, K.D.V.H. and De Vriend, H.J. 2005. Turbulence characteristics in sharp open-channel bends. *Physics of Fluids*, **17**, 055102, https://doi.org/10.1063/1.1886726
- Blanckaert, K. and Graf, W.H. 2001. Mean flow and turbulence in open-channel bend. *Journal of Hydraulic Engineering*, **127**, 835–847, https://doi.org/10.1061/(ASCE)0733-9429(2001)127:10(835)
- Chauvet, H., Devauchelle, O., Métivier, F., Lajeunesse, E. and Limare, A. 2014. Recirculation cells in a wide channel. *Physics of Fluids*, **26**, 016604, https://doi.org/10.1063/1.4862442
- Constantinescu, G., Koken, M. and Zeng, J. 2011. The structure of turbulent flow in an open channel bend of strong curvature with deformed bed: insight provided

- by detached eddy simulation. *Water Resources Research*, **47**, W05515, https://doi.org/10.1029/2010WR010114
- Demers, S., Buffin-Bélanger, T. and Roy, A.G. 2011. Helical cell motions in a small ice-covered meander river reach. *River Research and Applications*, **27**, 1118–1125, https://doi.org/10.1002/rra.1451
- Devauchelle, O., Popović, P. and Lajeunesse, E. 2022. Viscous transfer of momentum across a shallow laminar flow. *Journal of Fluid Mechanics*, **932**, https://doi.org/10.1017/jfm.2021.1021
- Ettema, R. 2002. Review of alluvial-channel responses to river ice. *Journal of Cold Regions Engineering*, **16**, 191–217, https://doi.org/10.1061/(ASCE)0887-381X(2002)16:4(191)
- Ferreira da Silva, A.M. and Ebrahimi, M. 2017. Meandering morphodynamics: insights from laboratory and numerical experiments and beyond. *Journal of Hydraulic Engineering*, **143**, 03117005, https://doi.org/10.1061/(ASCE)HY.1943-7900.0001324
- Finnemore, E.J. and Franzini, J.B. 2002. Fluid Mechanics with Engineering Applications. McGraw-Hill Education.
- Galloway, J.M. and Nustad, R.A. 2012. Sediment Loads in the Red River of the North and Selected Tributaries near Fargo, North Dakota 2010–2011. Scientific Investigations Report No. 2012-5111. US Geological Survey, 1–46, https://doi.org/10.3133/sir20125111.
- Gautier, E., Dépret, T. *et al.* 2021. Fifty-year dynamics of the Lena River islands (Russia): spatio-temporal pattern of large periglacial anabranching river and influence of climate change. *Science of the Total Environment*, **783**, 147020, https://doi.org/10.1016/j.scitotenv.2021.
- Ghareh Aghaji Zare, S., Moore, S.A., Rennie, C.D., Seidou, O., Ahmari, H. and Malenchak, J. 2016. Estimation of composite hydraulic resistance in ice-covered alluvial streams. Water Resources Research, 52, 1306–1327, https://doi.org/10.1002/2015WR018096
- Guo, J. 2017. Eddy viscosity and complete log-law for turbulent pipe flow at high Reynolds numbers. *Journal of Hydraulic Research*, **55**, 27–39, https://doi.org/10.1080/00221686.2016.1212945
- Guo, J., Shan, H., Xu, H., Bai, Y. and Zhang, J. 2017. Exact solution for asymmetric turbulent channel flow with applications in ice-covered rivers. *Journal of Hydraulic Engineering*, 143, 04017041, https://doi.org/10.1061/(ASCE)HY.1943-7900.0001360
- Hanjalić, K. and Launder, B.E. 1972. Fully developed asymmetric flow in a plane channel. *Journal of Fluid Mechanics*, **51**, 301–335, https://doi.org/10.1017/ S0022112072001211
- Kang, S. and Sotiropoulos, F. 2011. Flow phenomena and mechanisms in a field-scale experimental meandering channel with a pool-riffle sequence: insights gained via numerical simulation. *Journal of Geophysical Research: Earth Surface*, **116**, F03011, https://doi.org/10.1029/2010JF001814
- Kirillin, G., Leppäranta, M. *et al.* 2012. Physics of seasonally ice-covered lakes: a review. *Aquatic Sciences*, **74**, 659–682, https://doi.org/10.1007/s00027-012-0279-y
- Koken, M., Constantinescu, G. and Blanckaert, K. 2013. Hydrodynamic processes, sediment erosion

- mechanisms, and Reynolds-number-induced scale effects in an open channel bend of strong curvature with flat bathymetry. *Journal of Geophysical Research: Earth Surface*, **118**, 2308–2324, https://doi.org/10.1002/2013JF002760
- Koyuncu, B. and Le, T. 2020. Secondary flow structures in natural channels under open and ice-coverage conditions. Paper presented at the 73rd Annual Meeting of the APS Division of Fluid Dynamics, Abstract P16.00001, 22–24 November 2020, Virtual.
- Koyuncu, B. and Le, T. 2021. On the structures of the icecovered flows in a bend. Paper presented at the 74th Annual Meeting of the APS Division of Fluid Dynamics, Abstract T29.00002, 21–23 November 2021, Phoenix, Arizona, USA.
- Koyuncu, B. and Le, T.B. 2022. On the impacts of ice cover on flow profiles in a bend. Water Resources Research, 58, e2021WR031742, https://doi.org/10.1029/ 2021WR031742
- Lane, S.N., Bradbrook, K.F., Richards, K.S., Biron, P.M. and Roy, A.G. 2000. Secondary circulation cells in river channel confluences: measurement artefacts or coherent flow structures? *Hydrological Processes*, 14, 2047–2071, https://doi.org/10.1002/1099-1085(20000815/30)14: 11/12<2047::AID-HYP54>3.0.CO;2-4
- Lauzon, R., Piliouras, A. and Rowland, J.C. 2019. Ice and permafrost effects on delta morphology and channel dynamics. *Geophysical Research Letters*, 46, 6574–6582, https://doi.org/10.1029/2019GL082792
- Lotsari, E., Kasvi, E., Kämäri, M. and Alho, P. 2017. The effects of ice cover on flow characteristics in a subarctic meandering river. *Earth Surface Processes and Landforms*, 42, 1195–1212, https://doi.org/10.1002/esp. 4089
- Métivier, F., Lajeunesse, E. and Devauchelle, O. 2017. Laboratory rivers: Lacey's law, threshold theory, and channel stability. *Earth Surface Dynamics*, **5**, 187–198, https://doi.org/10.5194/esurf-5-187-2017
- Nanson, G.C. and Huang, H.Q. 2017. Self-adjustment in rivers: evidence for least action as the primary control of alluvial-channel form and process. *Earth Surface Processes and Landforms*, **42**, 575–594, https://doi. org/10.1002/esp.3999
- Parker, G. 1978. Self-formed straight rivers with equilibrium banks and mobile bed. Part 1. The sand-silt river. *Journal of Fluid Mechanics*, **89**, 109–125, https://doi.org/10.1017/S0022112078002499
- Petrie, J. and Diplas, P. 2016. Evaluation of the logarithmic law of the wall for river flows. *River Research and Applications*, **32**, 1082–1093, https://doi.org/10.1002/rra.2920
- Petrie, J., Diplas, P., Gutierrez, M. and Nam, S. 2013. Data evaluation for acoustic Doppler current profiler measurements obtained at fixed locations in a natural river. *Water Resources Research*, **49**, 1003–1016, https://doi.org/10.1002/wrcr.20112
- Phillips, C.B. and Jerolmack, D.J. 2016. Self-organization of river channels as a critical filter on climate signals.

- Science (New York, NY), **352**, 694–697, https://doi.org/10.1126/science.aad3348
- Popović, P., Devauchelle, O., Abramian, A. and Lajeunesse, E. 2021. Sediment load determines the shape of rivers. *Proceedings of the National Academy of Sciences*, 118, e2111215118, https://doi.org/10.1073/pnas.2111215118
- Seizilles, G., Devauchelle, O., Lajeunesse, E. and Métivier, F. 2013. Width of laminar laboratory rivers. *Physical Review E*, 87, 052204, https://doi.org/10.1103/Phys RevE.87.052204
- Seizilles, G., Lajeunesse, E., Devauchelle, O. and Bak, M. 2014. Cross-stream diffusion in bedload transport. *Physics of Fluids*, **26**, 013302, https://doi.org/10. 1063/1.4861001
- Shen, C. and Lemmin, U. 1997. A two-dimensional acoustic sediment flux profiler. *Measurement Science and Technology*, **8**, 880, https://doi.org/10.1088/0957-0233/8/8/008
- Sukhodolov, A., Thiele, M., Bungartz, H. and Engelhardt, C. 1999. Turbulence structure in an ice-covered, sand-bed river. Water Resources Research, 35, 889–894, https://doi.org/10.1029/1998WR900081
- Teal, M.J., Ettema, R. and Walker, J.F. 1994. Estimation of mean flow velocity in ice-covered channels. *Journal of Hydraulic Engineering*, **120**, 1385–1400, https://doi. org/10.1061/(ASCE)0733-9429(1994)120:12(1385)
- Tsai, W.F. and Ettema, R. 1996. A Study of Ice-Covered Flow in an Alluvial Bend. IIHR Technical Report No. 376. Iowa Institute of Hydraulic Research, College of Engineering, The University of Iowa.
- Urroz, G.E. and Ettema, R. 1994. Application of twolayer hypothesis to fully developed flow in ice-covered curved channels. *Canadian Journal of Civil Engineer*ing, 21, 101–110, https://doi.org/10.1139/194-010
- van Balen, W., Blanckaert, K. and Uijttewaal, W.S. 2010. Analysis of the role of turbulence in curved open-channel flow at different water depths by means of experiments, LES and RANS. *Journal of Turbulence*, **11**, N12, https://doi.org/10.1080/14685241003789404
- Vionnet, C.A., Tassi, P.A. and Martín Vide, J.P. 2004. Estimates of flow resistance and eddy viscosity coefficients for 2D modelling on vegetated floodplains. *Hydrological Processes*, 18, 2907–2926, https://doi.org/10.1002/hyp.5596
- Wang, F., Huai, W., Liu, M. and Fu, X. 2020. Modeling depth-averaged streamwise velocity in straight trapezoidal compound channels with ice cover. *Journal of Hydrology*, 585, 124336, https://doi.org/10.1016/j. jhydrol.2019.124336
- Wang, F., Huai, W., Guo, Y. and Liu, M. 2021. Turbulence structure and momentum exchange in compound channel flows with shore ice covered on the floodplains. *Water Resources Research*, **57**, e2020WR028621, https://doi.org/10.1029/2020WR028621
- Yang, X., Pavelsky, T.M. and Allen, G.H. 2020. The past and future of global river ice. *Nature*, **577**, 69–73, https://doi.org/10.1038/s41586-019-1848-1